We are IntechOpen, the world's leading publisher of Open Access books Built by scientists, for scientists

4,800
Open access books available

122,000
International authors and editors

135M
Downloads

Our authors are among the

154
Countries delivered to

TOP 1%
most cited scientists

12.2%
Contributors from top 500 universities

CLARIVATE ANALYTICS BOOK CITATION INDEX INDEXED

WEB OF SCIENCE™

Selection of our books indexed in the Book Citation Index in Web of Science™ Core Collection (BKCI)

Interested in publishing with us?
Contact book.department@intechopen.com

Numbers displayed above are based on latest data collected.
For more information visit www.intechopen.com

15

Annealing Effects on the Particle Formation and the Optical Response

Akira Ueda*, Richard R. Mu and Warren E. Collins
Fisk University
USA

1. Introduction

We present two examples for annealing effects on the implanted ions in substrates: (1) Se in SiO_2 and (2) Au in MgO. For the first system, Se in SiO_2, we analyze the absorption edges for selenium quantum dots for samples with several doses and annealed at different temperatures. From the absorption edge data, we discuss the formation of Se particles. For the second system, Au in MgO, we have seen the change in surface plasmon resonance (SPR) energy by annealing in different atmospheres from reducing to oxidizing or vice-versa. In this system, we discuss the role of substrate interacting with the implanted ions.

2. Temperature dependence and annealing effects of absorption edges for selenium quantum dots formed in silica glass

We have fabricated Se nanoparticles in silica substrates by ion implantation followed by thermal annealing up to 1000°C, and studied the Se nanoparticle formation by optical absorption spectroscopy, Rutherford backscattering spectrometry, X-ray diffraction, and transmission electron microscopy. The sample with the highest dose ($1x10^{17}$ ions/cm^2) showed the naonparticle formation during the ion implantation, while the lower dose samples (1 and $3x10^{16}$ ions/cm^2) required thermal treatment to obtain nano-sized particles. The Se nanoparticles in silica were found to be amorphous. After thermal annealing, the particle sizes became larger than the exciton Bohr radius for bulk Se. Thus, the absorption edges for different doses approached the value of bulk after thermal annealing. The temperature dependent absorption spectra were also measured for this system in a temperature range from 15 to 300 K.

2.1 Overview of selenium

Selenium is a semiconductor that has been extensively studied in the past because of the applications in photovoltaic cells, rectifiers, xerography, and so on. Solid selenium is known to occur as four major allotropes: an amorphous, trigonal, and two monoclinic phases (Murphy et al., 1977). In the solid and liquid states, selenium exists in two kinds of unit structures: rings and chains. The monoclinic allotropes are composed of eight-membered

* Corresponding Author

rings in two different stacking patterns, while the trigonal selenium is composed of helical chains. The glassy selenium consists of a mixture of rings and polymeric chains. For the trigonal phase, bulk selenium has the band gap of 1.7-2.2 eV, while monoclinic phase has the band gap of 2.4-2.6 eV (Pankove, 1971). However, the values are varied in the literature and they are not yet well determined. It is also known that the temperature effect on the band gap of bulk selenium is relatively high ($[\Delta E_g/\Delta T]_P$ = -1.4x10^{-3} eV/K), compared with the other semiconductors (-2~7x10^{-4} eV/K).

Recently, quantum size effects on the optical properties on semiconductor nano-sized particles have been observed. The third-order optical susceptibility for small semiconductor crystallites is found to be very large (Hanamura, E. 1988). The nano-sized selenium quantum dots are expected to exhibit changes in electronic and vibrational characteristics due to the quantum size effects. The band gap is generally expected to be blue shifted from bulk value as the particle size decreases (Brus, L.E. ,1982).

2.2 Experimental method

Selenium ions were implanted into fused silica substrates (Corning 7940) at an energy of 330 keV with doses of 1, 3, 6, and 10 x 10^{16} ions/cm^2. The samples were annealed at 600, 800, and 1000^{o}C for 1 h in a 5%H_2 + 95%Ar atmosphere in a tube furnace. The optical absorption spectra were measured from 185 to 2500 nm with a dual beam spectrophotometer (Hitachi U-3501) before and after annealing. Reflectance spectra were measured using a refractive index matching fluid with the incident angle of 5^o. For temperature dependent measurements in the range of 15-300 K, we used a helium closed cycle type cryostat (Leybold, RGD 210) fitted with silica windows. The spectra were collected at 25 K intervals, which were monitored with a temperature controller (Lakeshore, 320 Autotuning). The errors due to the fluctuation in temperatures can be on the order of ±5 K. The depth profiles of the implanted layer were determined by Rutherford backscattering spectrometry (RBS) using 2.2 MeV He^{2+} ions. X-ray diffraction (XRD) and transmission electron microscopy (TEM) measurements were conducted to find the crystal structure and size of the Se quantum dots in silica glass.

2.3 Experimental results

The depth profiles of Se in fused silica measured by RBS are shown in Fig. 1. The shape of the ion concentration distribution is approximately Gaussian with a peak concentration located at 0.2 μm below the surface with a full width at half maximum of about 0.2 μm.

Fig.2(a) shows the transmission spectra of the as-implanted samples with four different Se doses, which were measured at RT. In the UV region, there are two absorption bands at ~250 nm and ~350 nm. The band at 350 nm can be clearly observed for 3 and 6 x 10^{16} ions/cm^2. The optical absorption edge changes for each dose. Fig. 2(b) shows the transmission spectra of the samples annealed at 1000^{o}C in a reducing atmosphere for 1 h, which were also measured at RT. The intensity of the band at ~350 nm is no longer resolved. On the other hand, the band at ~250 nm became stronger for the samples of 3, 6, 10 x 10^{16} ions/cm^2. After annealing the samples, X-ray diffraction measurements were carried out and demonstrated that the nanoparticles were in an amorphous phase. (The X-ray diffraction spectrum is not shown here.)

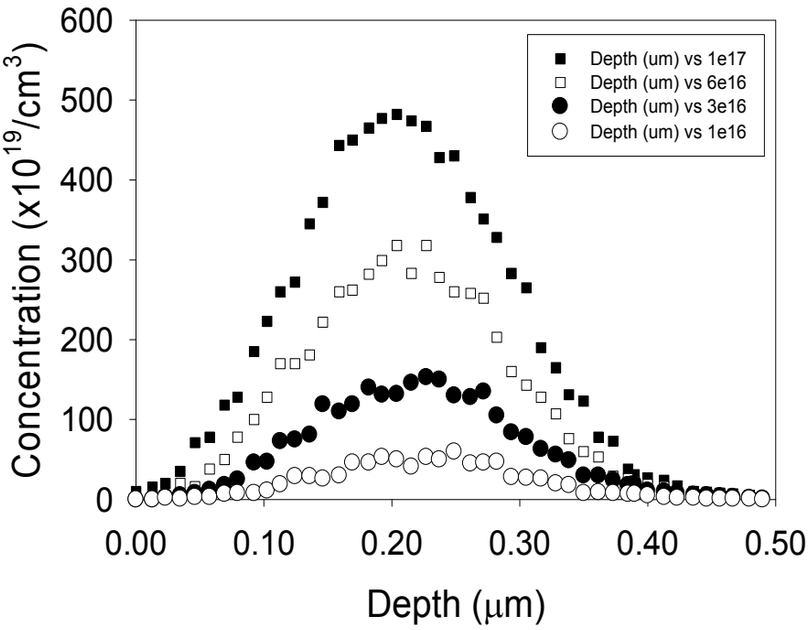

Fig. 1. The depth profile of Se ions in silica by RBS. (Ueda et al., 2007)

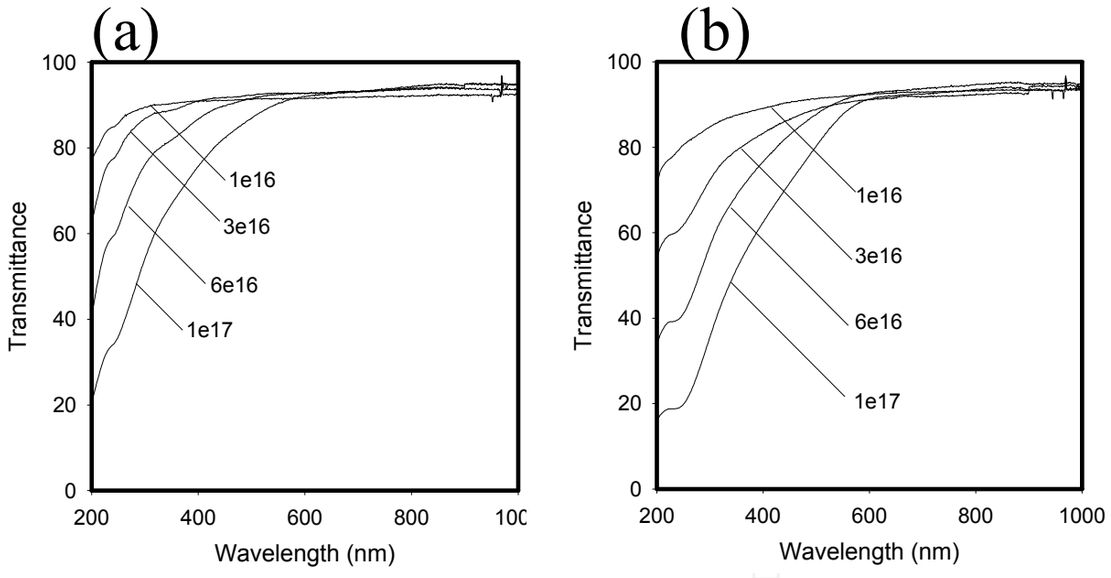

Fig. 2. Transmission spectra of Se/SiO_2 (a) as-implanted samples and (b) after annealing at 1000°C for 1 h.

Fig. 3 shows the transmission spectra of the samples with a dose of 1 x 10^{17} ions/cm^2 annealed at 600, 800, 1000°C in a reducing atmosphere for 1 h and the as-implanted sample measured at RT. According to these data, it is observed that the absorption edge is near 600 nm (~2 eV). (Ueda et al., 2007)

For the samples with a dose of 1x10^{17} ions/cm^2 annealed at 800 and 1000°C, the low-temperature absorption measurements were carried out between 15 K and 325 K, as shown

in Fig. 4. We repeated these measurements three times for each sample and the statistical uncertainty can be on the order of ±0.05 eV for the absorption edge. However, the trend is clear for the temperature effects and annealing temperature dependence of absorption edge. The sample annealed at 1000°C has the lowest absorption edge at each temperature as compared to the other annealing. As the temperature approaches 0 K, the traces become flat. The coefficient of temperature effects at 300 K for every trace is on the order of ~$10x10^{-4}$ eV/K (10.8, 12.4, $9.0x10^{-4}$ eV/K for as-implanted, annealed at 800°C, and 1000°C, respectively), which is similar to literature values of bulk Se (-14 x 10^{-4} eV/K) (Pankove, 1971).

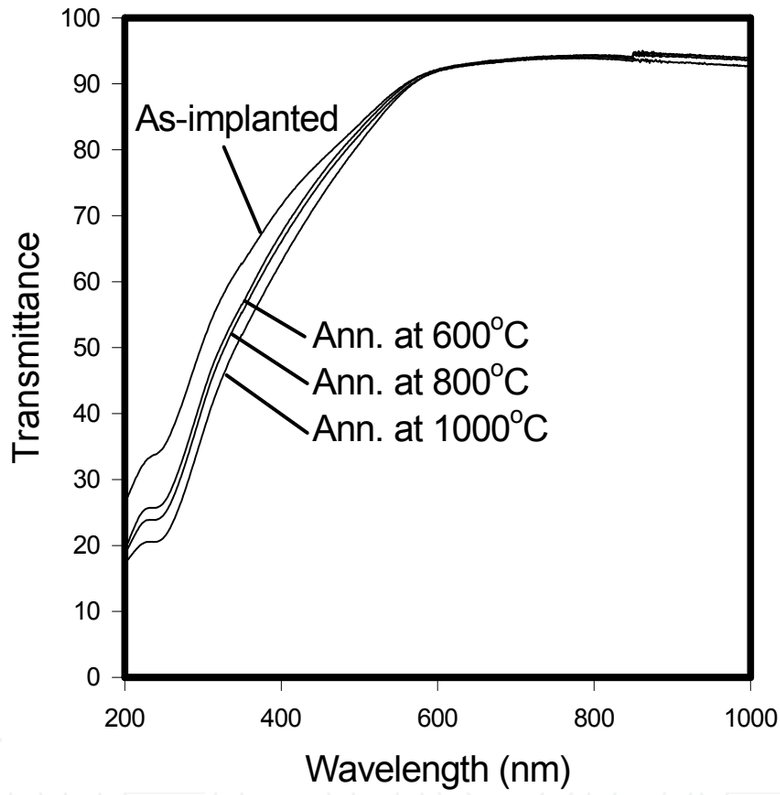

Fig. 3. Transmission spectra of the samples with a dose of $1x10^{17}$ ions/cm^2. (Ueda et al., 2007)

Transmission electron micrographs have been taken for the samples with a dose of $1x10^{17}$ ions/cm^2. Fig.5 (a), (b), and (c) show nanocrystal formation in samples annealed at 600°C, 800°C, and 1000°C, respectively. The micrographs indicate that the size of the Se nanoparticles at the peak of Se concentration distribution is about 10 nm for every sample. However, there exist smaller sized particles (≤ 3 nm) in the samples annealed at lower temperatures, which indicates that annealing of samples at higher temperature causes the increase of particle sizes, while smaller particles played a role as a material source (Ostwald Ripening).

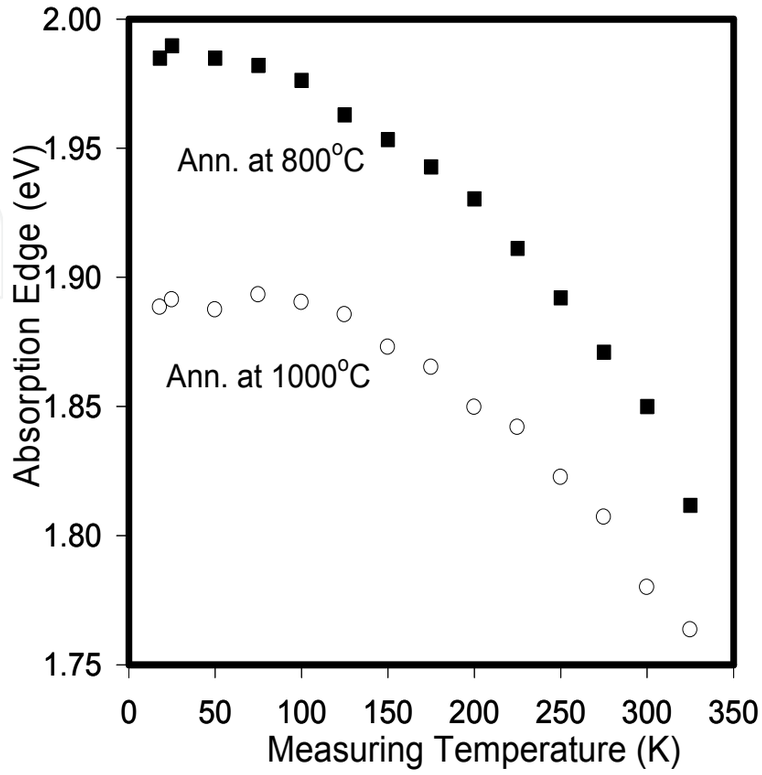

Fig. 4. Temperature dependence of absorption edge measured in the range of 15-325 K. (Ueda et al., 2007)

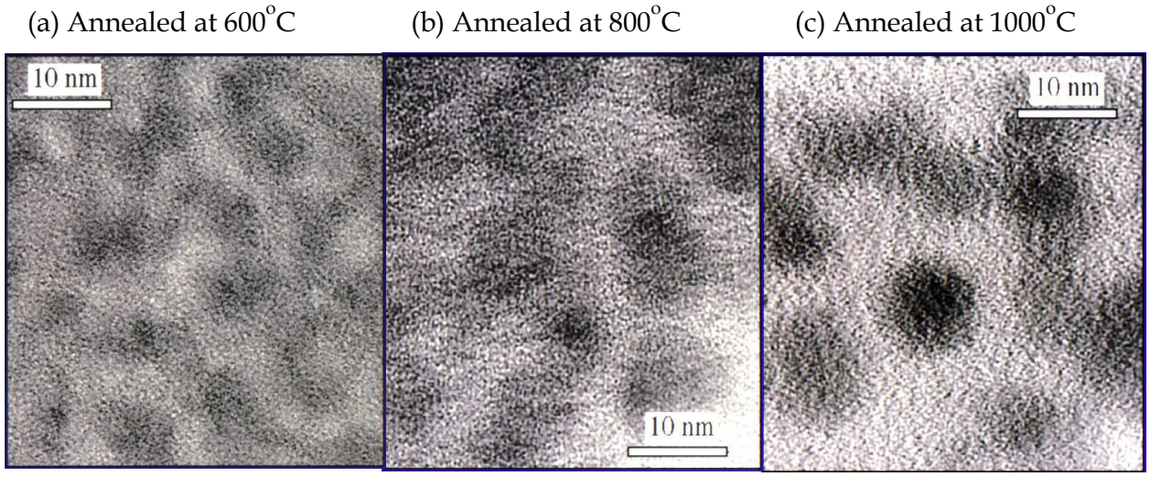

Fig. 5. High-resolution TEM micrographs of Se nanocrystals in SiO_2 annealed at (a)600°C, (b)800°C, and (c)1000°C. (Ueda et al., 2007)

2.4 Discussions

Considerable work has been published on the optical absorption in amorphous semiconductors, however its interpretation is not straightforward. As is well known, amorphous semiconductors do not have a sharp band gap unlike that for crystalline semiconductors. In amorphous materials, there exist some states smeared into the band gap of corresponding crystalline semiconductors. Most of the experimental data on amorphous semiconductors in the strong absorption region were found to be in agreement with the so-called Tauc law (Nagels et al., 1995; Tauc, 1972):

$$\alpha h\nu = C\left(h\nu - E_g\right)^2 \tag{1}$$

where $h\nu$ is the photon energy, E_g. is the optical band gap, C is a constant. For the thin Se films, Nagels *et al.* (Nagels et al., 1995) used the transmission spectrum of the sample together with the reflectance spectrum for a single surface of the sample to determine the band edge. For our samples, Se is an implanted layer in the glass and not a film, however, we utilized Nagels' formalism as the first approximation for band edge determination. By inverting the following relationship among the transmittance, the reflectance, and the absorption coefficient, we can obtain the absorption coefficient α:

$$T = \frac{(1-R)^2 exp(-\alpha d)}{1 - R^2 exp(-2\alpha d)} \tag{2}$$

where T is the transmittance, R is the reflectance for a single surface, and d is the sample thickness. Since T and R are functions of wavelength, α is also a function of wavelength. Inserting α into the Tauc equation and taking the square root, we plotted $(\alpha d h\nu)^{1/2}$ versus $h\nu$. A linear fitting was carried out for the linear segment corresponding to the absorption edge. Then the intersection of the extrapolated line with the photon energy axis ($\alpha = 0$) gives us the optical band gap E_g.

Fig. 6(a) shows the Tauc plots of the spectra of Fig. 2(a) for the as-implanted samples. The samples with doses of 6 and 10x10^{16} ions/cm^2 have relatively long linear segments, allowing for extrapolation of the linear part. We obtained E_g = 2.29 eV and 2.12 eV for 6 and 10x10^{16} ions/cm^2, respectively. For the 3x10^{16} ions/cm^2 sample, the linear segment is shorter, leading to more uncertainty in the band edge, however, an approximate value of 3.11 eV was obtained. For 1x10^{16} ions/cm^2, it is difficult to find the linear part probably because the implanted ion dose is not sufficient to form nanoparticles yet. Hence, it does not follow the Tauc Law. In this sample, the implanted ions are expected to be in the form of isolated ions or small clusters. Fig. 6(b), (c), and (d) show the Tauc plots of the spectra for the samples annealed at 600, 800, and 1000^{o}C, respectively. In Fig. 6(d), every spectrum has a linear part corresponding to the absorption edge, indicating that these spectra follow Tauc's law. The extrapolated lines cross the photon energy axis (α = 0) around one point: For 1, 3, 6, and 10 x 10^{16} ions/cm^2, the values of E_g are 1.83, 1.70, 1.77, and 1.75 eV, respectively. In Figs. 6(b) and (c), it is apparent that the onset of absorption edge shifts to larger values for the lower ion doses (1, 3, 6, and 10 x 10^{16} ions/cm^2).

According to the Tauc analysis for the samples of 10x10^{16} ions/cm^2, the absorption edges are 1.75, 1.81, 1.82, and 2.12 eV for the samples annealed at 1000^{o}C, 800^{o}C, 600^{o}C, and as-implanted, respectively. Although these absorption edges are similar to each other, the

sample annealed at higher temperature has a lower energy gap. These results indicate that for the highest dose samples (1x10^{17} ions/cm^2) the sizes of nanoparticles become sufficiently large to be greater than the exciton Bohr radius of bulk Se even during the ion implantation. Since the melting and boiling points of Se are relatively low (T_m = 217^{o}C and T_b = 685^{o}C) and ion implantation can cause a temperature increase in the substrate, this temperature increase may lead to the formation of large nanoparticles.

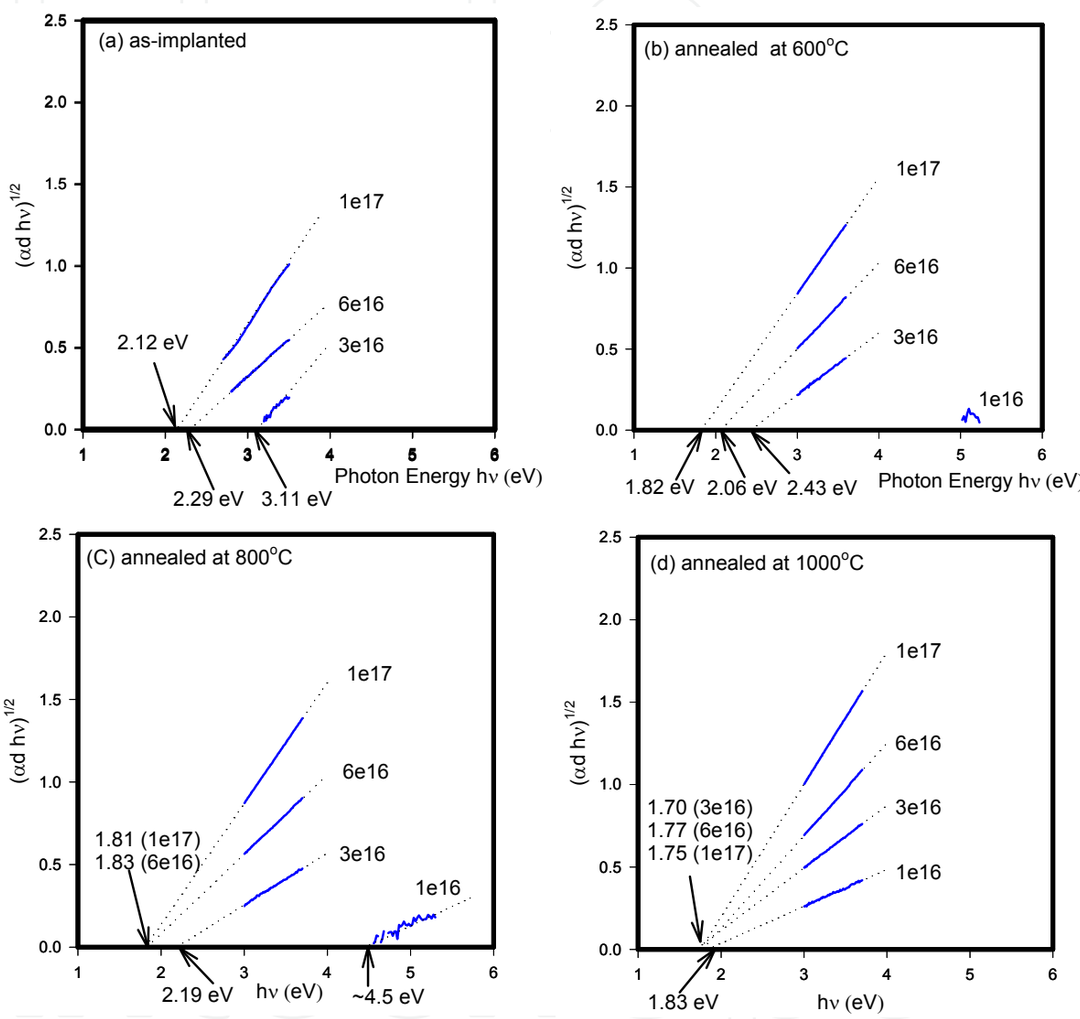

Fig. 6. Absorption edges of Se nanoparticles in silica by Tauc Analysis. (a) as-implanted, (b) annealed at 600^{o}C, (c) annealed at 800^{o}C, and (d) annealed at 1000^{o}C. (Ueda et al., 2007)

Such colloid formation during ion implantation has been reported previously for Ga implanted in glass (Hole et al., 1995). For the lower dose samples (1 and 3 x 10^{16} ions/cm^2), however, according to the results shown in Figs.6(a)-(d), the temperature rise during the implantation is not sufficient to form the final "ripened" size of nanoparticles that was obtained by annealing at 1000^{o}C.

The summary of the annealing temperature dependence on the optical absorption edges for each dose is given in Fig.7. There is no data point of as-implanted for the dose of 1 x 10^{16}

ions/cm^2. As we can see the trend in Fig.7, we may control the size of Se particles by annealing low dose samples (1 x 10^{16} ions/cm^2) at relatively low temperature between 200^{o}C and 800^{o}C for a certain time.

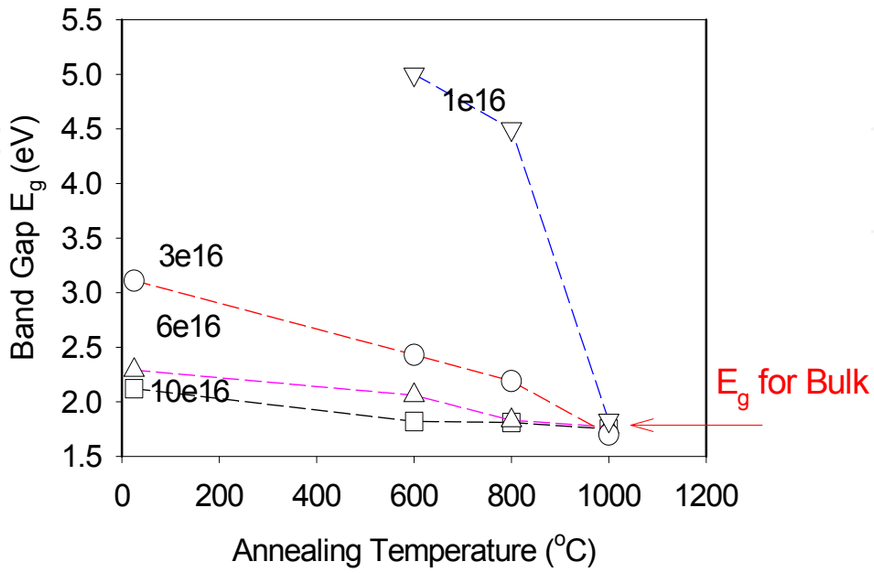

Fig. 7. The summary of Tauc Analysis; the optical absorption edges are given as functions of annealing temperature with annealing time of 1 hour. (Ueda et al., 2007)

The TEM observation is consistent with the results of the absorption edges, because the absorption edge for all samples annealed at 1000^{o}C is similar and the size of the particles should reflect the absorption edge, as mentioned before (Brus ,1982). However, according to the estimation by Huber (Huber & Huber, 1988), who impregnated porous Vycor Glass with Se to investigate the quantum confinement effects of Se, the exciton Bohr radius in bulk Se is 6.8 Å and the confinement energy is 0.011 eV for the cylindrical confinement of 50 Å in diameter. For 10 nm sized nanoparticles, the exciton radius is too small to experience quantum confinement and the energy shift corresponds to ~0.003 eV according to Brus' theory (Brus,1982), which can be neglected for absorption edge. The value of the Bohr radius, however, may not be reliable because the values of electron effective mass for Se have not been established yet in the literature. If the exciton Bohr radius is relatively larger than 6.8 Å, the smaller nanoparticles can contribute to shifting the absorption edge.

For the lower dose samples, however, the annealing treatment strongly affects the absorption edges because the nanoparticle formation requires more time or a higher temperature to reach the final size distribution. Since the annealing time was fixed at 1 h, the annealing temperature mainly controlled the sizes of the particles in this study.

2.5 Conclusions for this section

We have fabricated Se nanoparticles in silica substrates by ion implantation followed by thermal annealing. The Se nanoparticles are found to be amorphous. The sample with the highest dose (1x10^{17} ions/cm^2) showed the naonparticle formation even during ion implantation, while the lower dose samples (1 and 3x10^{16} ions/cm^2) did not. After thermal

annealing of the samples, the Se particle sizes become larger than the exciton Bohr radius for bulk Se. Thus, the absorption edges for different doses approached a common bulk value after thermal annealing. The TEM measurements for lower dose samples annealed at several temperatures will clarify the evolution of the nanoparticles. The temperature dependent spectra were also measured in a temperature range from 15 to 325 K. The value of $\left[\Delta E_g/\Delta T\right]_P$ is on the same order as the one for bulk. For the lower dose samples, the annealing treatment strongly affects the absorption edges. Since the annealing time was fixed at 1 h, the annealing temperature mainly controlled the sizes of the particles in this study. As we can see the trend in Fig.7, we may control the size of Se particles by annealing low dose samples (1 x 10^{16} ions/cm^2) at relatively low temperatures between 200°C and 800°C for a certain time.

3. Annealing effects on the surface plasmon of MgO implanted with gold

Gold ion implantation was carried out with the energy of 1.1 MeV into (100) oriented MgO single crystal. Implanted doses were 1, 3, 6, and 10 x 10^{16} ions/cm^2. The gold ion irradiation resulted in the formation of gold ion implanted layer with a thickness of 0.4 μm and defect formation. In order to form gold colloids from the as-implanted samples, we annealed the gold implanted MgO samples in three different kinds of atmospheres: (1)Ar only, (2)H_2 and Ar, and (3)O_2 and Ar. The annealing over 1200°C enhanced the gold colloid formation which shows surface plasmon resonance band of gold. The surface plasmon bands of samples annealed in three kinds of atmospheres were found to be at 535 nm (Ar only), 524 nm (H_2+Ar), and 560 nm (O_2+Ar). The band positions of surface plasmon can be reversibly changed by an additional annealing. Fe^{3+} impurities in MgO samples are utilized to monitor the degree of reduction of the samples due to annealing. From the absorption measurements of Fe^{3+} band, the diffusion constants of oxygen vacancies (F-centers) was obtained. We found that the shifts of the surface plasmon bands are correlated to the oxygen vacancy concentration and that F_n-center (aggregates of F-centers) is responsible for the shifting. According to the experimental results, we propose a model to explain the shift of surface plasmon band.

3.1 Overview of the surface plasmon resonance for small metal particles

In recent years, optical nonlinearity of small metal particles in dielectric materials has been paid much attention because of the possibility of the fast nonlinear response. The decreasing of materials to nanometer size often leads to significant changes in optical, structural, and thermodynamic properties. The appearance of the surface plasmon (SP) resonance for metal colloid reduced to the nanometer scale is one example of how the optical properties of metals change when they are reduced in size. To form nanometer sized metal particles, we used ion implantation methods (White, 1989). Metal colloid doped glasses, for example, show high optical nonlinearity, and are attractive candidates for utilization in optical devices (Fukumi, 1994; Haglund, 1992). The enhancement of the third order optical susceptibility depends on the intensity and frequency of the SP resonance of the metal colloids. According to Mie's scattering theory and the effective medium theory (Perenboom, 1981), we can predict the SP resonance frequency ω_{SP} if we know the dielectric functions of the metal colloid $\varepsilon(\omega)$ and the host material ε_m. As a first-order approximation, the following equation gives us the SP resonance frequency ω_{SP} (Perenboom, 1981; Kreibig & Vollmer, 1995):

$$\varepsilon(\omega_{SP}) + 2\varepsilon_m = 0 \quad (3)$$

We have previously reported on the SP resonance of gold nanoparticles in several substrates: Al_2O_3 (sapphire), CaF_2, and Muscovite mica (Henderson et al., 1995, 1996). MgO is also a material widely used in optics, such as windows and coatings. Although many of the alkaline earth oxides are hygroscopic and thus not widely used in optical systems, MgO is relatively insoluble, hard, and durable. Moreover, MgO is a good transparent material in the range between 300 nm and 7000 nm, and the optical absorption edge has been measured to be about 7.8 eV (160 nm) (Briggs, 1975). Transition metals, for example Fe^{3+}, are common multivalent impurities in MgO with order of 50 ppm. Absorption bands due to Fe^{3+} are found at 210 and 285 nm in MgO (Briggs, 1975). It has reported that the bands around 250 nm are related to F-center (248 nm) and F^+-center (252 nm), whose absorption bands overlap each other at room temperature (RT). F-center is defined as an oxygen vacancy with two trapped electrons, while F^+-center is defined as an oxygen vacancy with one electron. They can be created, for example, by neutron- and electron-irradiation or Mg-vapor-deposition at high temperature, which is so called additively colored crystal (Chen et al., 1969a, 1969b, 1967). The bands caused by neutron- and electron-irradiation can be annealed out at 600°C, while these bands generated by Mg-vapor-deposition could not be annealed out until the annealing temperature reaches the region of 1000-1200°C. The reason for this is as follows: in the sample, excessive Mg^{2+} ions are introduced from Mg vapor at 1800°C and then the Mg ions migrate into the MgO bulk to cause oxygen ion vacancies because of excessive Mg ions. In this case there exist no interstitial oxygen ions in the system, while neutron- or electron-irradiated samples have interstitial oxygen ions to re-combine to oxygen vacancies. The oxygen interstitials are mobile even below 600°C, while oxygen ion vacancies are immobile below 900°C (Chen et al., 1969a, 1969b, 1967). In this paper, we mainly report on how the annealing atmosphere affects to the SP resonance.

3.2 Experimental methods

MgO single crystal (15x15x0.5 mm^3) oriented (100) were obtained from two venders (Harrick Scientific and Commercial Crystal Laboratories). The major impurities are Fe^{3+} of ~100 ppm and Al^{3+} of ~40 ppm. The samples are implanted with 1.1 MeV gold $^{197}Au^+$ with doses of 1, 3, 6, and $10x10^{16}$ Au ions/cm^2 at RT. The depth profile of gold concentration was measured by Rutherford Backscattering Spectrometry (RBS), using 2.4 MeV α particles. Thermal annealing was carried out with a tube furnace at temperatures between RT and 1300°C in a reducing (10%H_2+90%Ar), an oxidizing (10%O_2+90%Ar), and an inert atmosphere (100%Ar) flow. The transmission spectra were measured between 185-3200 nm with a UV-Vis-NIR double beam spectrophotometer (Hitachi, U-3501).

3.3 Experimental results

3.3.1 Rutherford ackscattering Spectrometry (RBS) and TEM image

The RBS spectra show that the depth profile of gold is similar to the Gaussian distribution, whose peak concentration is located about 0.4 μm from the surface (The spectra are not shown here). The distribution is slightly asymmetric, which has a longer tail into the sample than surface side. The dominant gold ions are located within 1.0 μm region from the surface of (100) MgO with thickness of 0.5 mm. According to the results of RBS with the [100]-

channeling direction and the tilted angle measurements, MgO surface has not been amorphized.

Fig. 8 shows a TEM image of gold nanocrystals fabricated in MgO single crystal by ion implantation with a post annealing. The shape of the gold nanocrystals is cubic and they align along the crystal axis of host MgO [100]. This shape indicates that implanted ions interact with host materials during particle growth.

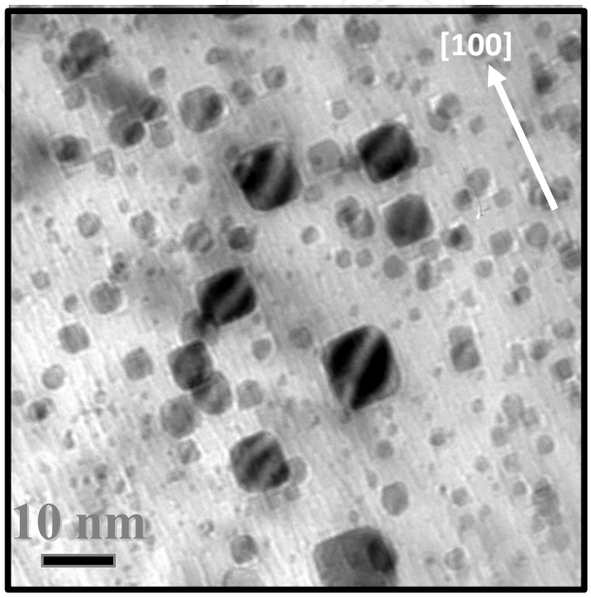

Fig. 8. TEM micrograph of MgO implanted with gold ions. (Cited from our paper, Bryant, E. M. et al., 2001)

3.3.2 Transmission of as-implanted samples

The transmission spectra of as-implanted Au/MgO samples and an unimplanted MgO sample (called "virgin MgO") are shown in Fig.9. The virgin sample (a) has high transmittance region (85% transmittance, 15% loss is mainly due to the reflection at both surfaces) down to 350 nm, and below 320 nm the transmittance suddenly drops due to Fe^{3+} ion impurities whose absorption bands are located at 285 nm and 210 nm. The spectra (b), (c), (d), and (e) are the transmission spectra for the gold implanted samples with doses of 1, 3, 6, and 10 $x10^{16}$ ions/cm^2, respectively. Every spectrum from (b) to (e) has a broad absorption band at 576 nm, which can be attributed to F_n-center (aggregates of F-centers) due to the irradiation damage by ion implantation (Weber, 1986). As the gold dose increases, the transmittance decreases in the range between 300 nm and 1000 nm, mainly due to scattering from small gold particles. The color of the as-implanted samples is dark brownish. Below 300 nm, the Fe^{3+} band is overlapped with the F- and F^+- center bands (at 248 nm and 252 nm).

3.3.3 Transmission of annealed samples

Fig.10 shows two sets of spectra of Au/MgO samples with the dosage of $6x10^{16}$ ions/cm^2 for sequentially annealed in both (a) reducing atmosphere [RA] and (b) oxidizing atmosphere

[OA]. The annealing temperature and time for each spectrum are shown in Fig.10. The band at 576 nm disappeared after annealing at 500°C in both atmospheres. It was reported by Chen et al. that the band at 576 nm was completely annealed out at 600°C. (Chen et al., 1969a, 1969b, 1967). Between 200°C and 1000°C, weak broad bands appeared around 340 and 365 nm. When the annealing temperature reached 1200°C, a strong broad band

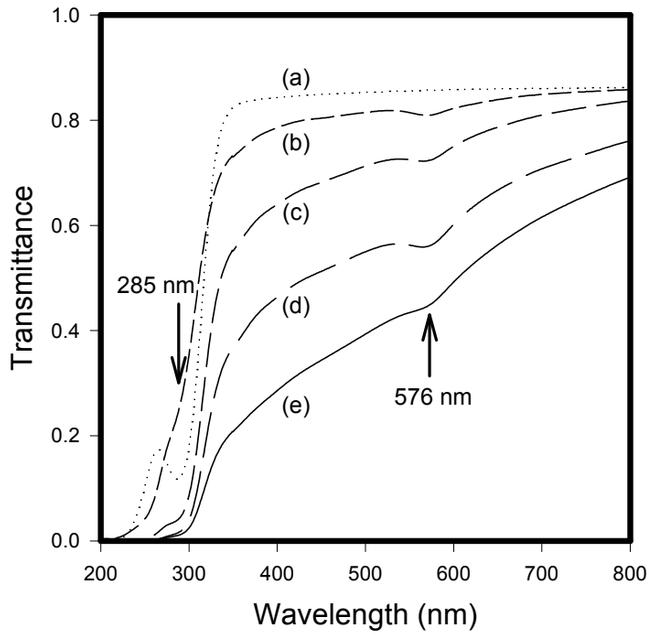

Fig. 9. Transmission spectra of (a) virgin MgO and as-implanted MgO with 1.1 MeV Au of (b) $1x10^{16}$, (c) $3x10^{16}$, (d) $6x10^{16}$, and (e) $1x10^{17}$ ions/cm^2. (Ueda et al., 1998)

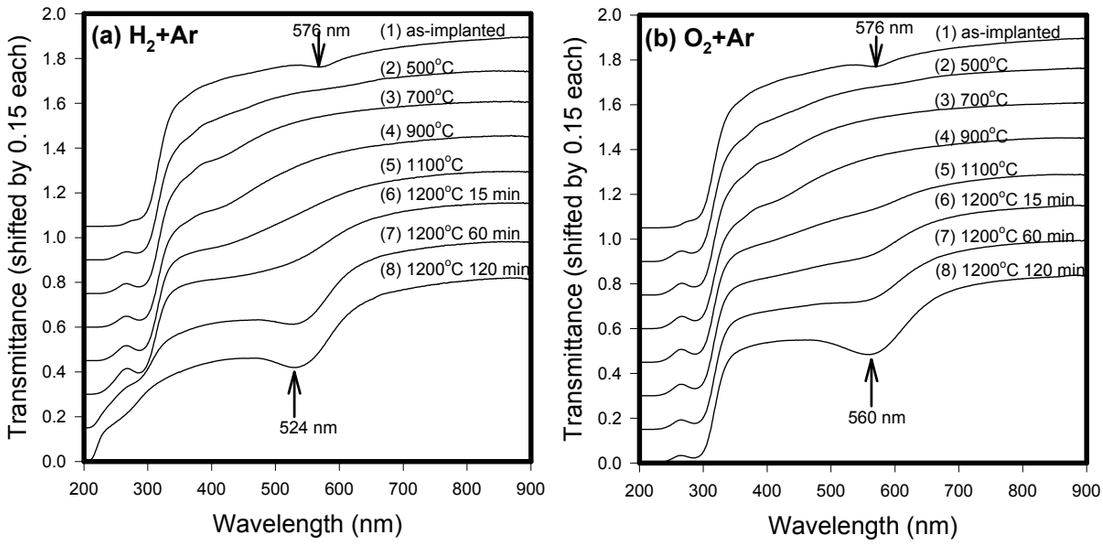

Fig. 10. Temperature development of transmission spectra of Au implanted in MgO annealed in (a)H_2+Ar and (b)O_2+Ar. In order to see easily, each spectrum has been vertically offset. (Ueda et al., 1998)

appeared at 524 nm for the samples annealed in the reducing atmosphere and at 560 nm for the oxidizing atmosphere, which are attributed to the SP resonance of gold colloids. As the annealing time increased at 1200°C, the SP bands became stronger and stronger, which indicates that at this temperature (1100 -1200°C) the implanted gold ions begin to diffuse and aggregate to form metallic colloids. In the case of the annealing in the reducing atmosphere, as shown in Fig.10(a), the Fe^{3+} band at 285 nm became weaker at high temperatures. It is coincident that oxygen vacancies become mobile at this temperature, as mentioned before (Chen et al., 1969a, 1969b, 1967).

3.3.4 Measurement of Fe^{3+} band as a monitor for creation and annihilation of F-centers

In order to investigate the correlation between the SP resonance and the reduction of the samples, we measured the transmission spectra of Fe^{3+} band at 285 nm of a virgin MgO sample that was sequentially annealed in the similar way to the previous annealing of gold implanted samples from RT to 1200°C. The Fig.11(a) shows the spectra of virgin MgO annealed in reducing atmosphere: the spectrum (a) is for the virgin MgO before annealing. Spectra (b), (c), and (d) are of the same sample after sequential annealing at 1000°C, 1100°C, and 1200°C, respectively, for 15 min each. Spectra (e) to (i) are of the same sample additionally annealed at 1200°C for 15 min for each step. During annealing between 200°C and 900°C with a step of 100°C for 15 minutes each, the spectra did not exhibit any significant changes (they are not shown in the figure.) After annealing at 1200°C for 90 minutes in total, (i) of Fig.11 (a), the surface of the sample became slightly cloudy. However, before it became cloudy, the Fe^{3+} band at 285 nm became weaker and weaker. Apparently, the Fe^{3+} ions were reduced to Fe^{2+} ions in the reducing atmosphere at high temperature, which resulted in an increased transmittance to 75% at 285 nm (Briggs, 1975). After annealing in the reducing atmosphere, we switched the atmosphere to O_2+Ar. The transmittance suddenly dropped just after annealing at 1200°C in the oxidizing atmosphere for 15 minutes, spectrum (j), as shown in Fig.11(b). We assume that Fe^{3+}ions uniformly distributed in the entire sample before annealing and that the reducing reaction occurs at the surface and proceeds to inside the sample until Fe^{3+} ions are completely converted to Fe^{2+} ions in reducing atmosphere. When annealing the samples in the oxidizing atmosphere, the conversion from Fe^{2+} to Fe^{3+} has taken place, as shown in Fig.11(b). However, this does not mean that both hydrogen and oxygen atoms diffuse into the sample. According to Griggs' experiments, the annealing MgO samples in several atmospheres showed that the gas used for annealing did not diffuse into the sample using deuterium gas (Briggs, 1975). In the reducing atmosphere at high temperature, a hydrogen molecule takes an oxygen atom at the surface with forming a water molecule, and leaves an oxygen vacancy with two electrons (F-center) behind, with giving one electron to an Fe^{3+} ion to form an Fe^{2+} ion if there exist Fe^{3+} ions nearby (Briggs, 1975; Yager & Kingery, 1981a, 1981b; Ueda et al., 2001a). In the case where Fe^{3+} ions do not exist near the surface, oxygen vacancies with electrons (F- or F^+-center) diffuse into the sample. (The diffusion of oxygen vacancies into the sample means that oxygen ions diffuse out from the sample.) At lower temperature this reaction occurs only at the surface with low rate and will not continue to react because oxygen vacancies are not mobile at low temperature (<1000°C). This is consistent with our observation that the spectra Fe^{3+} absorption decreases only at high temperature ($\geq$1200°C). In the oxidizing atmosphere, oxygen vacancies are filled with oxygen atoms, and an oxygen takes an electron from Fe^{2+} to convert it to Fe^{3+}. Oxygen ions diffuse into the sample when the temperature is high enough to make oxygen vacancies mobile.

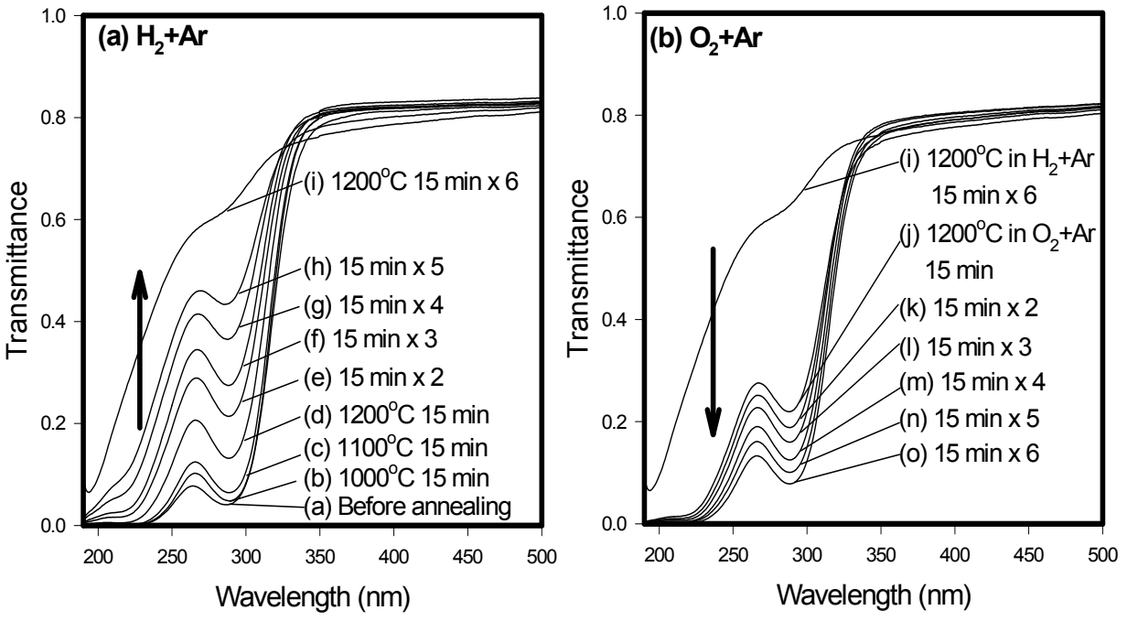

Fig. 11. Transmission spectra of virgin MgO annealed in (a) H_2+Ar and (b) O_2+Ar in the range of the Fe^{3+} absorption band. Cited from (Ueda et al., 2001)

3.3.5 Annealing temperature dependence of Fe^{3+} bands

A single virgin MgO crystal was annealed at 1200°C in O_2+Ar atmosphere for 5 hours to prepare a starting sample (the sample state O). The sample was then annealed in the reducing atmosphere for 5 h and transmission spectra were obtained at each temperature from 400°C to 1300°C with a step of 100°C to evaluate the degree of reduction as a function of annealing temperature. The sample annealed at 1300°C in the reducing atmosphere for 5 h is called as the sample state R. The sample (state R) was subsequently annealed in an oxidizing atmosphere for 5 h at each temperature from 400°C to 1300°C. This measurement is similar to the results shown in Fig.10, however, the annealing time and temperatures are different.

The area under Fe^{3+} absorption band at 285 nm was integrated for each temperature from RT (25°C) to 1300°C. In Fig.12, the annealing temperature dependence of the Fe^{3+} band is plotted for the samples annealed in both reducing and oxidizing atmospheres. Trace (1) shows the integrated band intensity as a function of annealing temperature under the reducing atmosphere, started with the sample state O. The integrated intensity of the Fe^{3+} band did not change until the annealing temperature reached 900°C. At this temperature, Fe^{3+} started to be reduced to Fe^{2+}. The reduction of Fe^{3+} then indicates the creation of oxygen vacancies, as will be presented. The band completely disappeared at 1300°C. This sample (sample state R) was used as the starting sample for annealing in the oxidizing atmosphere. Trace (2) shows that the Fe^{3+} band did not appear until the annealing temperature reached 900°C, and at 1000°C the sample started to be oxidized. The Fe^{3+} absorption band completely recovered at 1300°C.

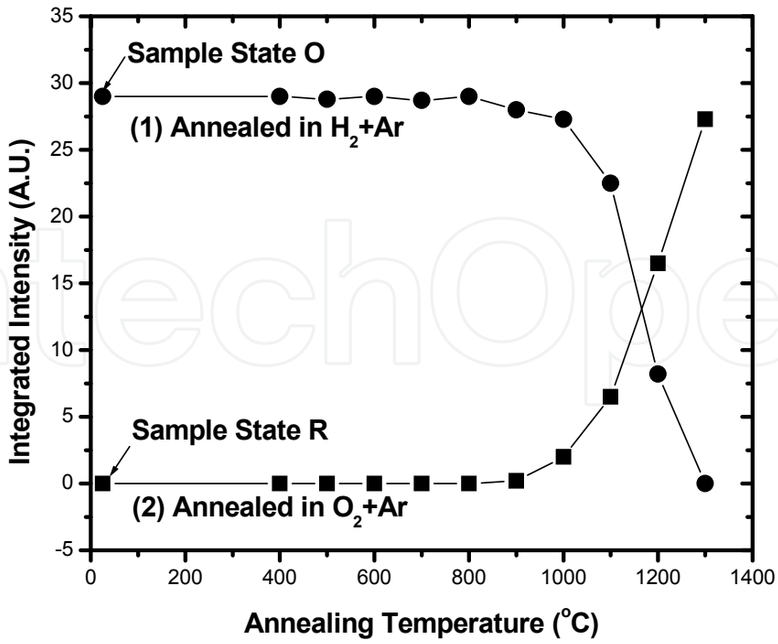

Fig. 12. Annealing temperature dependence of Fe^{3+} band in (1)H_2+Ar and (2)O_2+Ar. The starting sample for (1) was the oxidized state O, and that for (2) was the reduced state R. (Ueda et al., 2001)

3.3.6 Correlation between Fe^{3+}-band and F_n-band at 575 nm

After annealing the sample (state O) in the reducing atmosphere, an absorption band developed at 575 nm. Fig.13 shows the temperature dependence of the Fe^{3+} and 575 nm-bands. The intensity of the Fe^{3+} decreased as the annealing temperature increased, while the absorption at 575 nm increased. The band at 575 nm has been observed previously for MgO irradiated with neutrons and ions (Chen, 1969; B. Henderson & Bowen, 1971; Evans et al., 1972), and was attributed to aggregates of F-centers. Therefore, the correlation between the reduction of Fe^{3+} and the development of 575 nm-band suggests that the reduction of Fe^{3+} coincides with the creation of F-centers. Fig.13(b) shows temperature dependence of 575 nm-band.

3.3.7 Diffusion of oxygen vacancies

From the similar transmission data of virgin MgO annealed in reducing atmosphere for 5 hours at each temperature, we can estimate the diffusion behavior (Ueda et al., 2001a). The reason we took a longer annealing time of 5 hours is to establish the thermodynamic equilibrium at each temperature. The transmission spectra were converted to absorbance, and the absorption bands around 285 nm are integrated for each temperature from 800°C to 1200°C. Since below 700°C we did not see any significant changes, these data below 700°C are not useful to estimate the diffusion constants. The ratio (A/A_0) of the integrated absorbance at each temperature to that at RT can be related to the amount of the Fe^{3+} in the sample at each temperature. According to Fick's law, the diffusion constant is given by

$$\frac{d}{2}\left(1-\frac{A}{A_0}\right) = (D_0 t)^{1/2} exp\left(-\frac{E_a}{2kT}\right) \quad (4)$$

Here, d is the sample thickness (0.5 mm), and the annealing time t should be taken 5 hours (18 000 sec). Taking the logarithm of both sides and plotting these quantities versus 1/2T, we can obtain the values of E_a and D_0, as shown in Fig.14(a). A linear fitting of the plot gave values of E_a=3.08 $\pm$0.18eV and D_0 =3.63 x10^{10} μm^2 s^{-1}. The value of the activation energy is between the values for F^+- and F-centers (2.72 eV and 3.13 eV, respectively) that Kotomin *et al.* theoretically calculated (Kotomin et al., 1996). From these experimental values obtained, we re-plot the diffusion length as a function of annealing temperature in Fig.14(b). See ref. (Ueda et al., 2001a) for the detailed explanation.

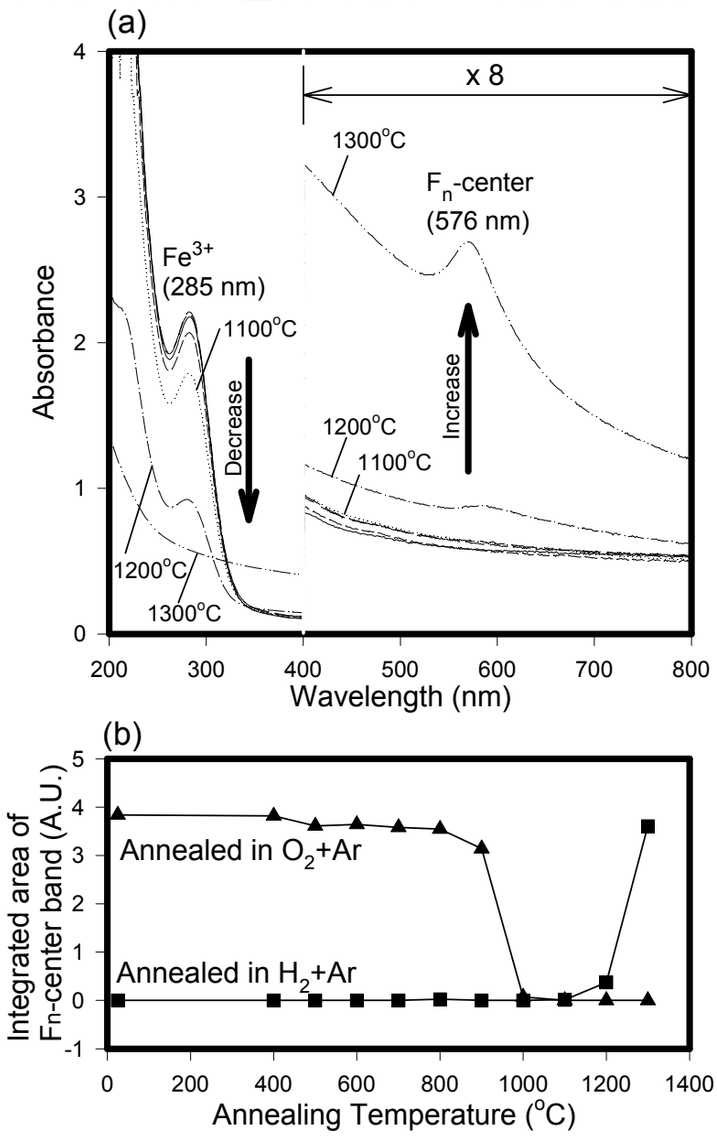

Fig. 13. (a) The temperature dependence of Fe^{3+} and 575 nm-bands during annealing in the reducing atmosphere. Fe^{3+} band decreased as annealing temperature increased, while 575 nm-band developed. (The vertical scale was magnified in the range of 400-800 nm by a factor of 8.) (b) Integrated area of 575 nm-band as a function of annealing temperature for both cases of annealing in O_2+Ar and H_2+Ar. Cited from (Ueda et al., 2001)

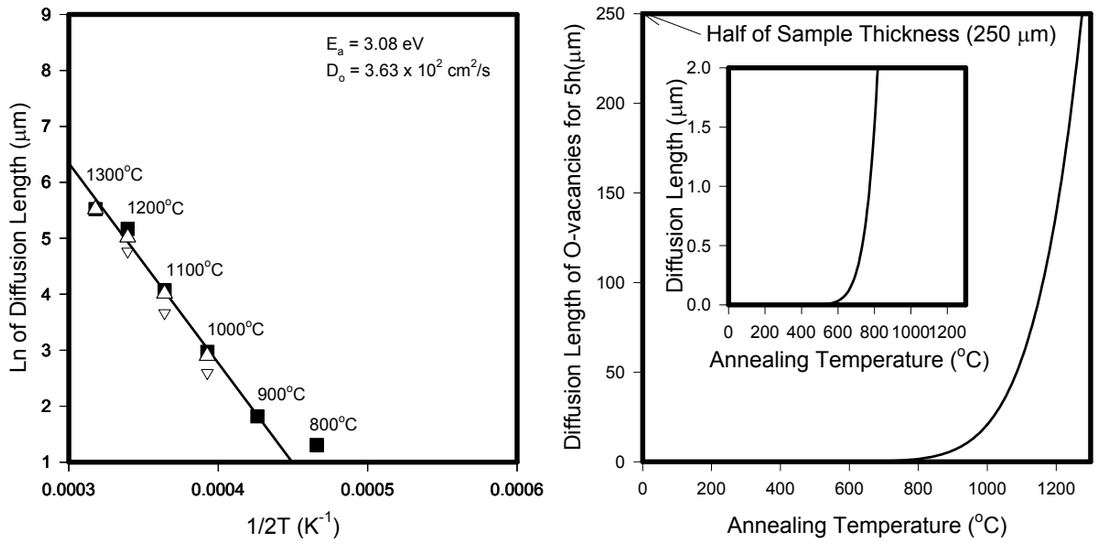

Fig. 14. (a) Linear fitting for the estimation of diffusion constants. (b) Diffusion length of oxygen vacancies as a function of annealing temperature for 5 h, using the values of the diffusion coefficient and the activation energy obtained from this study.(Ueda et al., 2001)

According to this plot, the diffusion of oxygen vacancies started around 900°C. (In the inset, the vertical scale is little magnified to see the small change.) This is consistent with the data which Chen *et al.* found that the oxygen vacancies in MgO become mobile around 1000°C (Chen et al., 1969a, 1969b, 1967). Note that this reduction process of MgO is essentially reversible, according to the data of Fe^{3+} transmission measurements, as shown later.

3.3.8 Annealing atmosphere dependence of surface plasmon band of Au in MgO

The Au implanted MgO samples showed SP bands after annealing at high temperature ($T \geq$ 1200°C), as mentioned previously. The SP band positions depend on the annealing atmospheres. To confirm the annealing atmosphere dependence of the SP band position, we sequentially annealed an implanted sample (Au/MgO with dose of $10x10^{16}$ inos/cm^2) at 1200°C in (1)Ar only, (2)O_2+Ar, (3)H_2+Ar, and (4)O_2+Ar again for 2 hours each. (1)After annealing in Ar only, SP appeared at 535 nm. (2)After annealing in O_2+Ar, SP shifted to 560 nm. (3)Annealing in H_2+Ar made SP shift to 524 nm. (4) Again, after annealing in O_2+Ar, SP moved back to 560 nm. From these results, the SP position is reversibly depending on the annealing atmosphere (Ueda et al., 1997).

To investigate this annealing atmosphere dependence of SP position, we annealed one piece of MgO implanted with gold ($1x10^{17}$ ions/cm^2) with a piece of virgin MgO as a reference at 1200°C in O_2+Ar atmosphere for 5 hours as a starting sample , whose SP position was 560 nm. These samples were annealed in the reducing atmosphere for 5 hours at each temperature from 400°C to 1300°C to find the SP position as a function of annealing temperature. In Fig.15(a), the trace (1) presents the SP position change under the reducing condition: Below 700°C, the SP position stayed at 560 nm, and SP position started to gradually change to the shorter wavelength from 800°C up to 1300°C. The final SP position was 527 nm, which was slightly longer wavelength than that stated in previous paragraph

(Ueda et al., 1997). Then this sample was annealed in the oxidizing atmosphere for 5 hours each at certain temperature from 400°C to 1300°C. In Fig.15(a), the trace (2) presents the SP position change: Below 700°C, the SP position stayed at 527 nm, and SP position started to suddenly change to the longer wavelength (~560 nm) between 800°C and 900°C. The SP position essentially stayed at about 560 nm above 900°C up to 1300°C. The final SP position was 563 nm, which is also slightly longer wavelength than that mentioned previously (Ueda et al., 1997). This sample was then annealed in the inert atmosphere (Ar only) in the same way as previous annealing. In the Fig.15(b), the trace (3) shows that the SP position essentially stayed around 560 nm, although there was a small dip at 1100°C. This sample was then first annealed at 1200°C in the reducing atmosphere for 5 hours to obtain the starting sample for annealing in the inert atmosphere, whose SP position was 523 nm as a starting SP position. In the Fig.15(b), the trace (4) shows that the SP position changed similarly to the trace (2) for annealing in O_2+Ar. From this similarity, the annealing in O_2+Ar and Ar only atmosphere are essentially thermal processes, which is the diffusion of oxygen vacancies from inside to the surfaces. On the other hand, the annealing in H_2+Ar atmosphere involves chemical reactions at the surface as well as thermal processes together. The chemical reaction mainly determines the rate of SP position change, which gradually changed from 800°C to 1300°C.

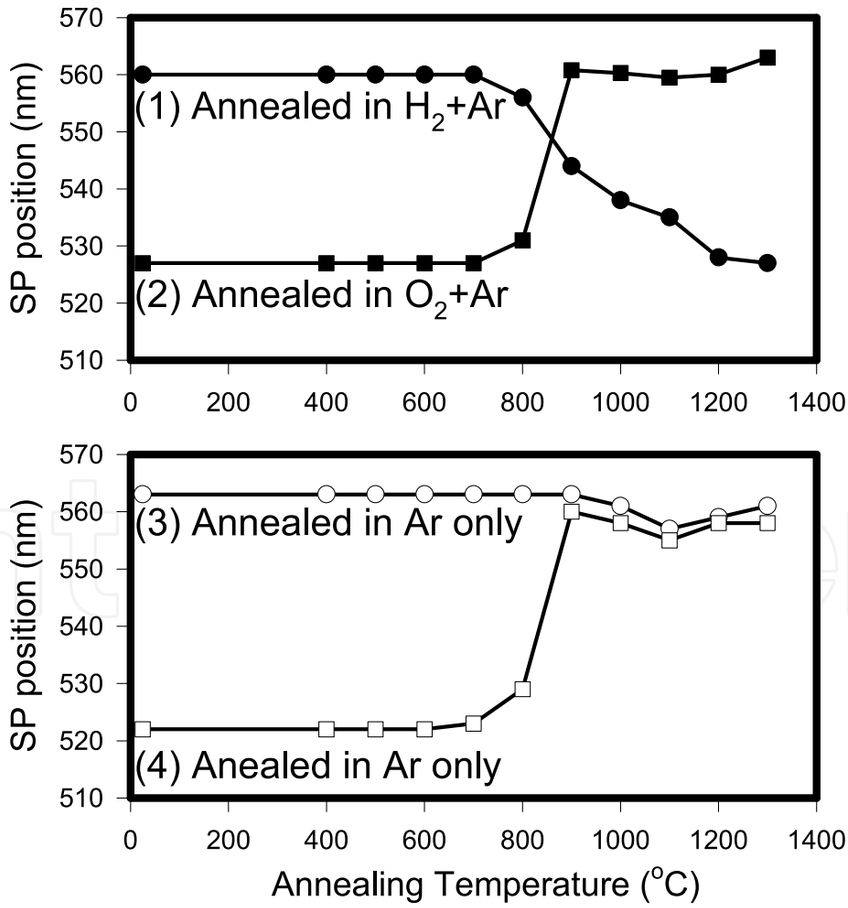

Fig. 15. Surface Plasmon (SP) position as a function of annealing temperature in different atmospheres. (Ueda et al., 1998)

3.3.9 Annealing temperature dependence of F_n-center and Fe^{3+}-bands

The temperature between 800°C and 900°C is a transition temperature for SP position shifting. This temperature, T_{OV}, is coincidently the temperature at which oxygen vacancies become mobile. Therefore, it is natural to mention that oxygen vacancies play an important role in the SP position shifting. A piece of virgin MgO was annealed with the previous annealing of the MgO implanted with Au ions for 5 hours at each temperature in order to see the roles of oxygen vacancies without the effects caused by the ion implantation. This is similar to the results shown in Fig.12, however, the annealing conditions are slightly

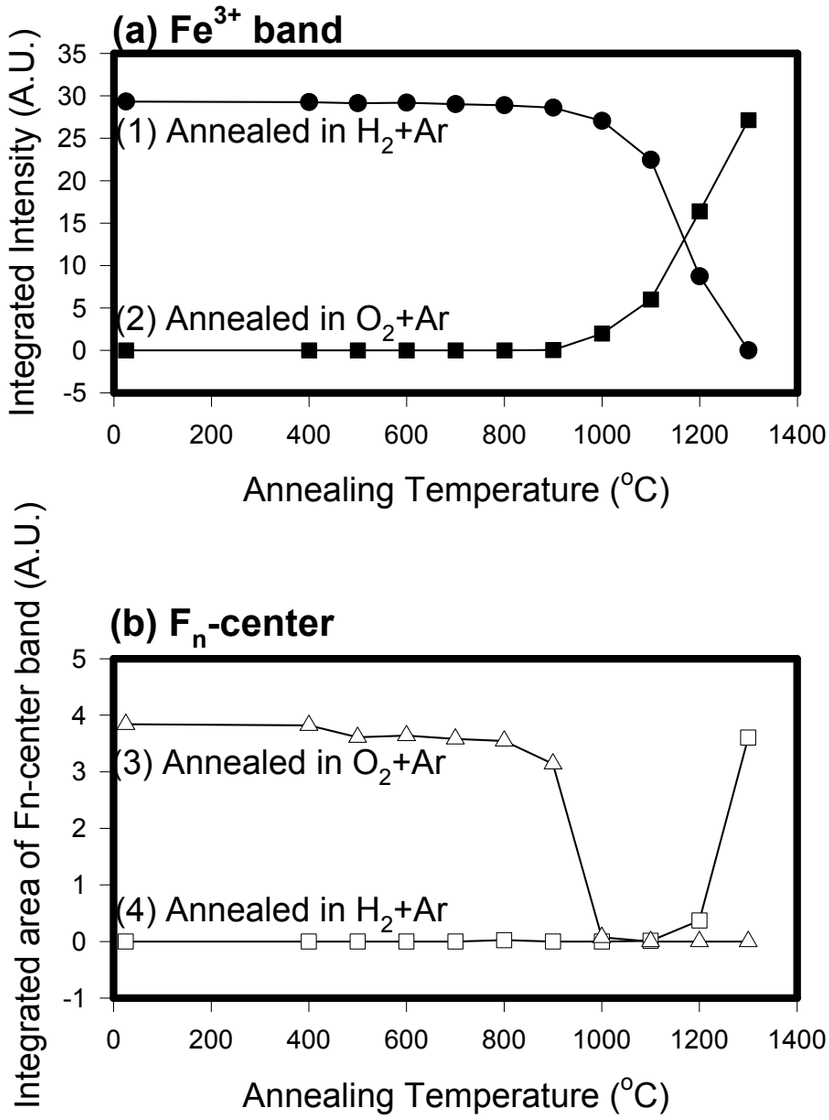

Fig. 16. Integrated intensities as a function of annealing temperature for Fe^{3+} and F_n-center bands. (Ueda et al., 1998)

different in the annealing time and temperatures. The transmission spectra were converted to absorbance, and the Fe^{3+} absorption band (285 nm) and F_n-center band (576 nm) are integrated for each temperature from RT (25°C) to 1300°C. In Fig.16(a), the annealing temperature dependence of Fe^{3+} band is plotted in both reducing and oxidizing atmosphere. The trace (1) shows the integrated band intensity as a function of annealing temperature under the reducing atmosphere, started with the sample annealed at 1300°C in the oxidizing atmosphere for 5 hours. The Fe^{3+} band did not change until the annealing temperature reached 900°C, and then at 1000°C the sample started to be reduced, which is the onset of F-center creation. The band completely disappeared at 1300°C, as shown. This final sample was used as the starting sample for the following annealing in the oxidizing atmosphere. Trace (2) shows that the Fe^{3+} band did not appear until the annealing temperature reached 900°C, and then at 1000°C the sample started to be oxidized, which is the beginning of F-center annihilation. The band completely came back at 1300°C, as shown. Trace (2) shows that oxidizing behavior was symmetrically going on with trace (1) for the reducing atmosphere. In Fig.16(b), the annealing temperature dependence of F_n -center band of the same sample is plotted. The traces (3) and (4) show the integrated F_n -center band intensity as functions of the annealing temperature under the oxidizing and reducing atmospheres, respectively. F_n-centers were gradually formed until 1200°C in the reducing atmosphere, however F_n -center were abruptly decomposed at relatively lower temperature (~T_{OV}), as shown. These traces (3) and (4) do not symmetrically behave, while the Fe^{3+} band did. It is a meaningful observation that Fn-center formation take place after enough F-centers are created, with comparison between traces (b)-(4) and (a)-(1), and that there were still F-centers in the entire sample even after F_n-centers were decomposed (1000-1200°C) because F_n--centers are aggregates of F-centers that play as the sources of F-centers during the decomposition of F_n-centers, with comparison between traces (b)-(3) and (a)-(2). Note that there is a similarity between the SP position shift and the F_n -center changes as functions of annealing temperature: Compare Fig.16(b)-(3) with Fig.15(a)-(2). There is a sudden change at T_{OV} (800-900°C) in SP position, while a sudden change occurs at 900-1000°C in F_n-center intensity. This is probably because the implanted gold layer is located at very shallow range from surface. This gold layer is about 1000 times thinner than whole sample thickness, so that before the entire sample has the final F_n -center distribution the implanted gold layer near the surface has already some degree of F_n -centers were formed.

3.4 Discussion of mechanism for surface plasmon resonance position shifts

We have seen the SP position of gold colloids can be shifted by annealing in a certain atmosphere. The SP position shifts reversibly by changing the annealing atmosphere from reducing to oxidizing or vice versa. Although the surface of the MgO sample becomes cloudy during annealing in the reducing atmosphere, this shifting is repeatable several times. Does the size or shape of gold colloid explain the SP position shifting? It is difficult to imagine that the size can be changed by annealing in an atmosphere after a gold colloid with a certain size had been formed. Since the state of as-implanted stage is not a thermodynamically equilibrium state that is metastable, the colloid formation during annealing is an irreversible process. Thus once most of the metastable gold ions formed larger colloids, they will not become smaller colloids at the temperatures where gold is

supposed to be liquid or solid phase and where the vapor pressure of gold is not considerably high. The shape of gold colloids may be changed by varying the surrounding environment of a colloid to lower the sum of surface energy for all facets of the colloid surface. However, since bulk gold forms fcc crystal structure, the shape of a colloid should be reflected in the cubic symmetry of MgO and the shape could be a truncated-octahedron or a sphere-like shape. Among these shapes, the SP position may not be so changed. Thus we need to seek the other explanations of the mechanism for the SP shifting. This reversibility suggests that there are two possible mechanisms to explain the SP position shifting according to the equation (1): (i) the dielectric function of host material (MgO) near gold colloids is influenced by the annealing. (ii) the dielectric function of gold colloids is changed by the annealing.

Using these values of ω_{SP} from experimental data, Eq.(3), and the optical constants of bulk gold from literature (Palik, 1991; Lide et al., 1998), we inversely calculated the local ε_m. These calculated values ε_m are supposed to be 3.01 (Ar only), 2.45 (H_2+Ar), and 3.90 (O_2+Ar), while the standard value of ε_m for MgO is 3.02. However, the dielectric constants ε_m of these samples measured by ellipsometry gave the following values: 2.99 (Ar only), 2.98 (H_2+Ar), and 2.99 (O_2+Ar). The reason why the calculated values ε_m of the samples vary so much and the experimental values are unchanged is as follows: If $-2\varepsilon_m$ and $\varepsilon(\omega)$ were drawn against wavelength, the crossing point satisfies the SP resonance condition according to Eq.(3). Fig.17 schematically depicts two possible situations. Since the dielectric function of gold is relatively steep compared with that of MgO host, horizontal lines present the function $-2\varepsilon_m$ and the steep function presents $\varepsilon(\omega)$. In Fig.17(a), the dielectric function $\varepsilon(\omega)$ of gold is assumed to be unchanged after annealing, and ε_m is supposed to be responsible for the SP shifting. On the other hand, in Fig.17(b) the dielectric function ε_m of MgO is assumed to be unchanged after annealing and $\varepsilon(\omega)$ is supposed to be responsible for the SP shifting. The experimental data support the case of Fig.17(b), that is, ε_m does not change so much and the dielectric function of gold colloids changes after annealing. In Fig.17(c), the model plot is given for the case where gold dielectric function's change is responsible for the shift of SP. However, there are other possibilities such as the combination of these two cases. Although the dielectric function ε_m of MgO did not change for samples annealed under different atmospheres, according to the ellipsometric measurement mentioned above, those values for ε_m were the averaged value of wide area of the sample, and the SP shift might be affected by the environment near gold particles.

Recalling the similarity between the SP shifting and the F_n-center intensity change for the case of annealing in oxidizing atmosphere, we had better compare Fig.15.(2) and Fig.16(3). Both traces suddenly change in the range of 800-1000°C. We can see the correlation between these two quantities: Just above the temperature where F_n-center intensity started to decrease, the SP position abruptly shifted to longer wavelength. On the other hand, for the case of the reducing atmosphere, SP shift gradually proceeded from 800°C and it saturated at 1200-1300°C, compared Fig.15.(1) with Fig.16(4). However, F_n-center apparently started to increase at 1200-1300°C. It is reasonable to imagine that F-centers and F_n-centers were formed near the surface due to the reduction of the MgO surface. Around the critical temperature T_{OV}, F-centers diffuse into the sample, while F_n-centers do not diffuse because F_n-center are too large to diffuse. Thus, the F-centers *evaporated* from F_n-centers near the

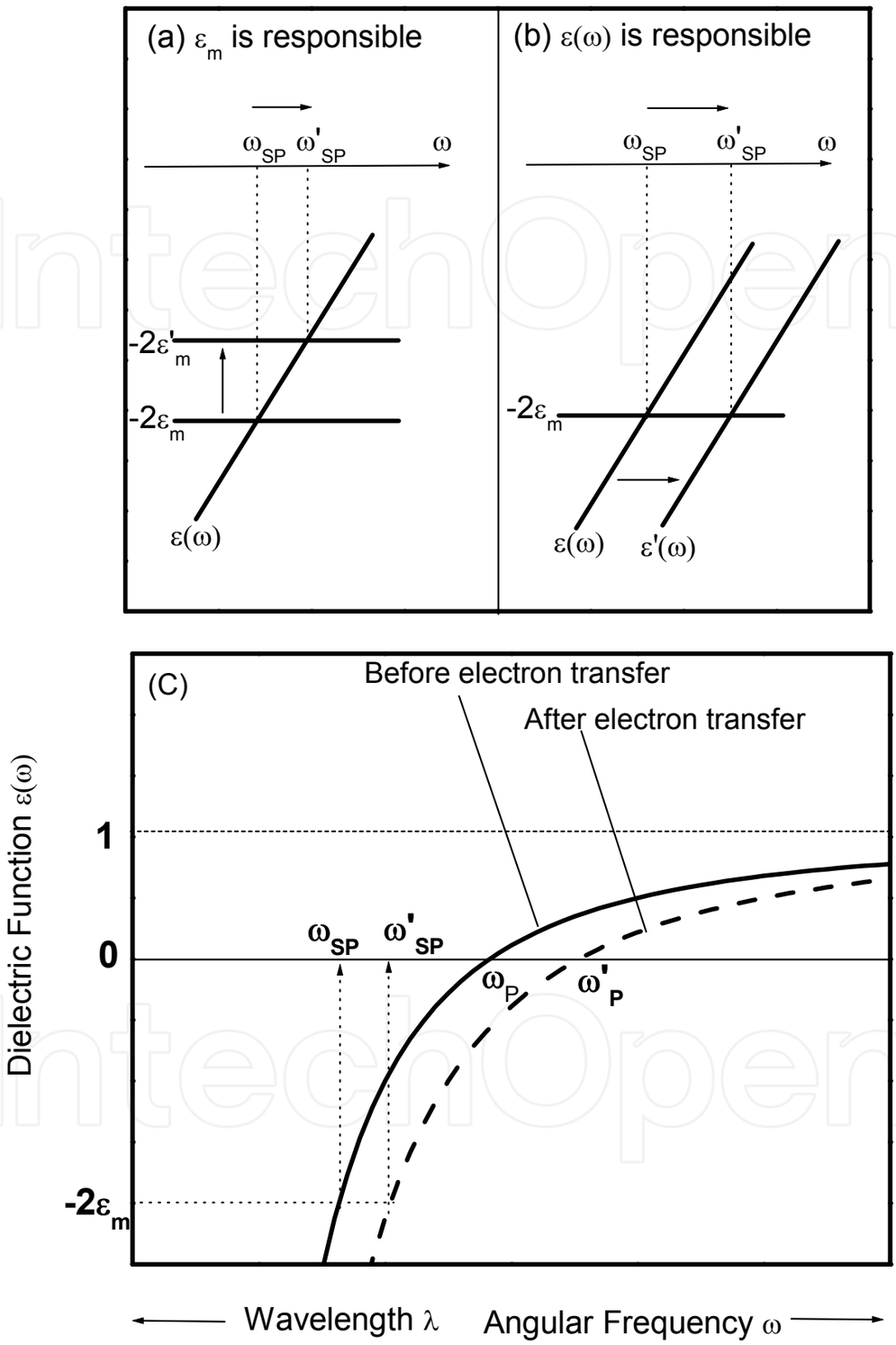

Fig. 17. Schematics for SP band shift situation. (a) the case where ε_m is responsible, (b) the case where $\varepsilon(\omega)$ is responsible, and (c) the model plot for case where $\varepsilon(\omega)$ is responsible for the shift of SP band.

surface can diffuse in, and the F-centers form their aggregates only when the concentration of F-centers reaches a threshold. However, until the F_n-centers and F-centers reach the equilibrium, the F_n-centers may be partly decomposed and then the evaporated F-centers diffuse into the sample according to the gradient of the concentration of F-centers. Thus, as we can see, at the very shallow surface near the implanted gold layer, the degree of F_n-centers gradually increase, which corresponds that SP position gradually changed until F_n-centers suddenly increased at 1200°C. However, between 800°C and 1200°C the evaporation and diffusion are in progress until the F-center concentration in the entire sample reaches the threshold to form F_n-centers around 1200°C.

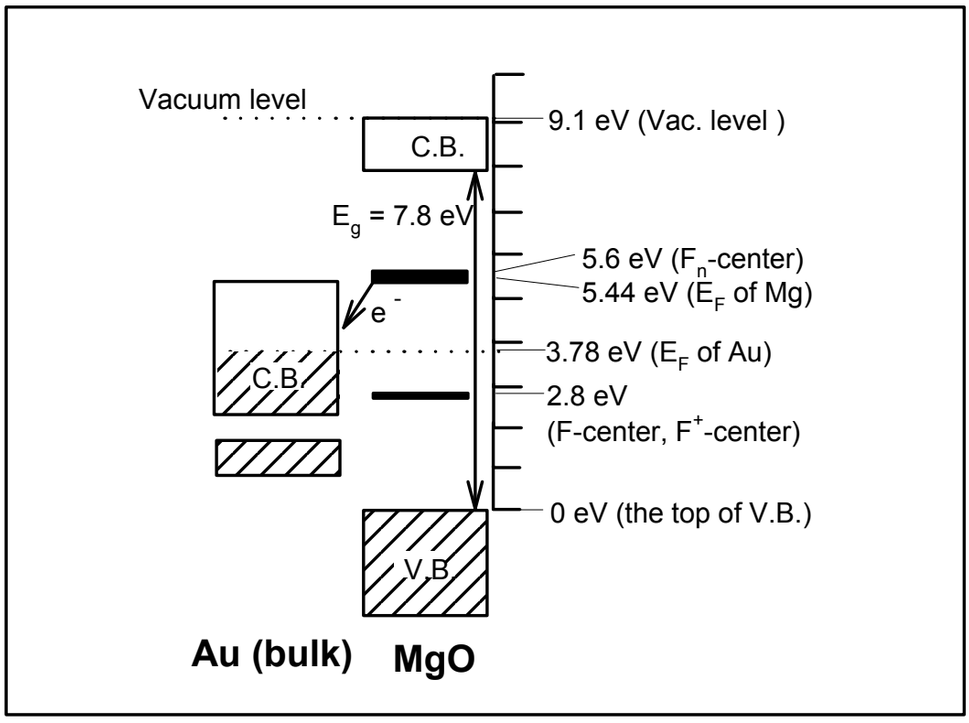

Fig. 18. Energy diagram of Au (bulk), MgO, Fn-center, F-center, and the other related energy levels. Relative positions are determined according to literature, as explained in text. (Ueda et al., 1998)

Let us consider how the dielectric function of gold colloid can change the value. F_n-center is defined as an aggregate of F-centers, which may be regarded as a metallic Mg colloid. In alkali halides irradiated with photons or electrons, metallic colloids were found as F-center aggregates (Fughes & Jain, 1979). If F_n-centers are formed close to gold colloids, electrons in the F_n-centers can transfer to the gold colloids because the Fermi level of bulk Mg metal is higher than that of bulk gold (Lide et al., 1998). The work function for bulk Mg and bulk gold are 3.66 eV and ~5.4 eV, respectively (Lide et al., 1998). The band gap of MgO is 7.8 eV and the vacuum level of MgO was found to be 9.1eV from the top of valence band by UPS (Tjeng et al., 1990). The energy levels of F- and F^+-centers are given by Chen et al. (Chen et al., 1969a, 1969b, 1967). The absorption band of F_n-center is located around 576 nm (2.15 eV) from our experimental data and literature values (Weber, 1986). Assuming that the final state of this transition is the bottom of the conduction band of MgO, we propose that the energy level for F_n-center is located about 2.2 eV below the bottom of the conduction band of MgO, which is 5.6 eV above the top of valence band. Summary of these data are shown in Fig.18. Note that the level of F_n-center is coincident with the Fermi level of bulk Mg metal, as mentioned before. The Fermi level of bulk gold is located much lower than the F_n-center level by 1.8 eV. Therefore, the electrons in F_n-center are able to transfer to gold colloids nearby. We did not consider the quantum confinement effect on electrons in gold colloids in order to estimate the energy scheme in Fig.18. The Fermi level of the gold colloids may have higher value than that of bulk gold, as shown in Fig.18.

Leaving this question at this stage, we would like to explain a simple mechanism of the dielectric function change of gold colloid due to electron transfer from F_n-centers to gold colloid, which correspond to Fig.17(c). In the free-electron gas model for metals, the dielectric function is given by the following equation (Kittel, 2005):

$$\varepsilon(\omega) = 1 - \frac{{\omega_p}^2}{\omega^2} \tag{5}$$

with the plasma frequency of gold colloid defined by, in SI units,

$${\omega_P}^2 = \frac{ne^2}{\varepsilon_0 m_e} \tag{6}$$

where e and m_e are the electron charge and mass, ε_0 is the permittivity of vacuum, and n is the electron density of a gold colloid we are considering. When some electrons in F_n-center are transferred into the gold colloid, the electron density of the gold colloid will increase so that the plasma frequency will increase. Fig.17(c) shows that the dielectric functions before and after electrons are transferred, in which the SP resonant frequencies are schematically given, according to the resonance condition: $\varepsilon(\omega_{SP}) = -2\varepsilon_m$. From this figure, we can see that the SP frequency blue-shifts after electrons are transferred. This is the case of the sample annealed in the reducing atmosphere and F_n-center plays a role of an electron injector.

Let n_0 be the electron density of a gold colloid in the oxidized MgO and n′ to be that of the same colloid in the reduced MgO. The potential difference between the Fermi level of gold

and F_n-center level is about $\Delta\varphi = 1.8\,eV$. To compensate this potential difference, electrons can transfer from F_n-centers to the gold colloid. Although our gold colloid has a cubic shape, we regard it as a sphere for simplicity and suppose that the radius of the gold colloid is r. Thus, the volume of this colloid is $V_{colloid} = 4\pi r^3/3$. Let the transferred charge be ΔQ, and then the change in the number of electrons in the gold colloid will be

$$\Delta N \equiv \frac{\Delta Q}{e} \tag{7}$$

The charge transferred ΔQ is related to the potential difference $\Delta\varphi$ (volt) as follows:

$$\Delta\varphi = \frac{\Delta Q}{4\pi\varepsilon_0 r} \tag{8}$$

Eliminating ΔQ from (7) and (8), we obtain

$$\Delta N = \frac{4\pi\varepsilon_0 r\Delta\varphi}{e} \tag{9}$$

Assuming that the electron density of gold colloid in oxidized MgO is similar to the one of bulk gold; n_0=5.9x10^{28} m^{-3} (Lide et al., 1998), the total number of electrons in the colloid is given by

$$N_0 = n_0 V_{colloid} = \frac{4\pi r^3 n_0}{3} \tag{10}$$

The ratio of ΔN to the total number of electrons of an neutral Au colloid, N_0, is

$$\frac{\Delta N}{N_0} = \frac{\left(\frac{4\pi\varepsilon_0 r\Delta\varphi}{e}\right)}{\left(\frac{4\pi r^3 n_0}{3}\right)} = \frac{3\varepsilon_0\Delta\varphi}{e n_0 r^2} \approx \frac{0.005}{r^{*2}} \tag{11}$$

Here, r^* is defined as a numerical part of r in nm as follows: $r = r^* \times 1\,nm$. The dielectric function for gold before transfer is given by Eq.(5) with (6):

$$\varepsilon(\omega) = 1 - \frac{{\omega_P}^2}{\omega^2}, \qquad {\omega_P}^2 \equiv \frac{n_0 e^2}{\varepsilon_0 m_e}. \tag{12}$$

From Eq.(3), The surface plasmon position ω_{SP} satisfies

$$\varepsilon(\omega_{SP}) = 1 - \frac{{\omega_P}^2}{{\omega_{SP}}^2} = -2\varepsilon_m \tag{13}$$

After the charge transfer, the dielectric function for gold can be given by

$$\varepsilon'^{(\omega)} = 1 - \frac{{\omega'_P}^2}{\omega^2}, \qquad {\omega'_P}^2 \equiv \frac{n'^{e^2}}{\varepsilon_0 m_e} \tag{14}$$

After the charge transfer, the surface plasmon position ω'_{SP} satisfies

$$\varepsilon(\omega'_{SP}) = 1 - \frac{{\omega'_P}^2}{{\omega'_{SP}}^2} = -2\varepsilon_m \tag{15}$$

Here, although ε_m may have been changed, for simplicity, we assume that ε_m stays the same. By subtracting Eq.(14) from Eq.(12) each side, we get

$$\frac{{\omega'_P}^2}{{\omega'_{SP}}^2} = \frac{{\omega_P}^2}{{\omega_{SP}}^2} \quad \rightarrow \quad \frac{{\omega'_{SP}}^2}{{\omega_{SP}}^2} = \frac{{\omega'_P}^2}{{\omega_P}^2} = \frac{n'}{n_0} = \frac{n_0 + \Delta n}{n_0} = 1 + \frac{\Delta n}{n_0} \tag{16}$$

The shift for ω_{SP} is qualitatively given by

$$\frac{\omega'_{SP}}{\omega_{SP}} = \sqrt{1 + \frac{\Delta n}{n_0}} \cong 1 + \frac{1}{2}\frac{\Delta n}{n_0} = 1 + \frac{1}{2}\frac{\Delta N}{N_0} \cong 1 + \frac{0.0025}{r^{*2}}. \tag{17}$$

If we insert $\Delta N/N \approx 0.005$ for r =1 nm, then the calculated shift for ω_{SP} becomes about 1 nm in wavelength, while the actual shift for ω_{SP} is more than 30 nm in wavelength. Inversely, if we seek for the radius that causes 30 nm wavelength shift, then we obtain r =0.2 nm. Therefore, this model may not explain the actual such large shift. Since the electric charge due to free electrons in a gold particle is compensated with the positive charge of nucleus, thus the gold particle is neutral as a whole. The transferred charge, however, is an additional negative charge, so the transferred charge should be located on the surface of the gold particle. This localized surface charge may play an important role.

3.5 Sectional summary

We have found that the annealing atmosphere affects the position of SP band of Au implanted in MgO. The SP band position of the sample annealed in the reducing atmosphere is found to be about 524 nm, and that for the sample annealed in the oxidizing atmosphere is about 560 nm. These SP position shifting is reversible and repeatable by changing the annealing atmosphere from reducing to oxidizing or vice versa. We observed that F_n-centers are created during annealing in the reducing atmosphere at higher temperature ($\geq$1200^{o}C). Since F_n-center energy level is higher than the Fermi level of the gold colloids in MgO, F_n-centers play the role of electron injectors. Therefore, the electron density of gold colloid is changed so that the SP position shifts. However, our simple model cannot quantitatively explain the experimental results. The shifting and its reversibility may be useful for application to the development of nonlinear optical devices or sensor of gases.

4. Conclusion

We have presented two kinds of samples: First, by using samples of Se implanted in silica glass, we explained Se particle growth by Tauc analysis of optical absorption spectra on annealed samples, where we mainly concentrate on the particle growth of implanted materials. Secondly, by using MgO single crystalline substrate implanted with Au ions, we explained the interaction between implanted species and host material MgO. We focused on the surface plasmon resonance position shift due to the state of host material MgO annealed under reducing and oxidizing atmospheres.

5. Acknowledgments

We gratefully acknowledge research that was previously supported by DOE grant No. DE-F605-94ER45521. The research at ORNL was sponsored by the Division of Materials Sciences, U. S. Department of Energy, under Contract No. DE-AC05-9OR22464 with Lockheed Martin Energy Systems. Currently, the authors are partly supported by US National Science Foundation NSF-CREST-CA: HRD-0420516 and NSF-STC CLiPS, grant No. 0423914.

6. References

Briggs, A., (1975), J. Mater. Sci. 10, 737.

Bryant, E.M., Ueda, A., Mu, R.R., Wu, M.H., Meldrum, A., Henderson, D.O., (2001) Mat. Res. Soc. Symp. Proc. Vol. 635, C1.5.1-6, MRS.

Brus, L.E. (1983) J. Chem. Phys. 79, 5566.

Brus, L.E. (1984) J. Chem. Phys. 80, 4403-4409.

Chen, Y., Williams, R.T. & Sibley, W.A., (1969). Phys. Rev. 182, 960.

Chen, Y. , Kolopus, J.L. & Sibley, W.A. (1969). Phys. Rev. 186, 865

Evans, B.D., Comas, J., & Malmberg, P.R. (1972). Phys. Rev. B 6, 2453.

Fughes, A.E.,& Jain, S.C., (1979) in: *Metal Colloids in Ionic Crystals, Advances in Physics*, 28, 717.

Fukumi, K., *et al.*, (1994). J. Appl. Phys. 75, 3075.

Haglund, R.F. *et al.*, (1992). Nucl. Instr. & Method, B65, 405.

Hanamura, E. (1988). Phys. Rev. B 37, 1273.

Henderson, B. & Bowen, D.H. (1971). J. Phys. C: Solid State Physics 4, 1487.

Henderson, D.O. *et al.*, (1995). J. Vac. Sci. Technol. B 13, 1198.

Henderson, D.O. *et al.*, (1996). J. Vac. Sci. Technol. A 14, 1199.

Hole, D.E. et al. (1995). J. Non-Cryst. Solids 180, 266.

Huber, C.A. & Huber, T.E. (1988). J. Appl. Phys. 64, 6588.

Kittel, C., (2005). *Introduction to Solid State Physics*, 7th Ed., John Wiley & Sons, ISBN: 047141526X, New Jersey, USA.

Kotomin, E.A., Kuklja, M.M., Eglitis, R.I., & Popov, A.I. (1996). Materials Science and Engineering B37, 212.

Kreibig, U. & Vollmer, M. (1995*). Optical Properties of Metal Clusters*, Springer Series in Materials Science 25, ed by Toennies, J.P., Springer-Verlag, Berlin, Heidelberg.

Lide et al. (1998) CRC Handbook of Chemistry and Physics, 79th Edition, eds by Lide, D.A. et al. CRC Press, ISBN: 0849304792, Boca Raton, Florida.

Murphy, K.E. et al. (1977). J. Appl. Phys. 48, 4122.

Nagels, P.; Sleeckx, E., Callaerts, R., & Tichy, L. (1995). Solid State Communications 94, 49.

Palik, E.D.(1991) "*Handbook of Optical Constants of Solids* I & II," Ed. by E.D. Palik, Academic Press, ISBN: 0125444222, San Diego, California, USA.

Pankove, J.I. (1971). *Optical Processes in Semiconductors*, Dover, ISBN: 0486602753, New York.

Perenboom, J.A.A.J., Wyder, P. & Meier, F. (1981). Phys. Rep. 78, 173.

Sibley, W.A. & Chen, Y. (1967). Phys. Rev. 160, 712.

Tjeng, L.H., Vos, A.R. & Sawatzky, G.A. (1990) Surface Science 235, 269.

Tauc, J. (1972). Chapter 5 of *Optical Properties of Solids,* ed. by F. Abeles, North-Holland Publishing Company, ISBN: 0720402042, Amsterdam.

Ueda, A., Mu, R., Tung, Y-S., Henderson, D.O., White, C.W., Zuhr, R.A., Zhu, J.G. & Wang, P.W. (1997). Materials Forum Vols. 239-241, pp. 675-678.

Ueda, A., Mu, R., Tung, Y-S., Wu, M.H., Collins, W.E., Henderson, D.O. Henderson, White, C.W., Zuhr, R.A., Budai, J.D., Meldrum, A., Wang, P.W., Li, Xi (1998), Nuclear Instrument and Methods in Physics Research B 141 261-267.

Ueda, A., Mu, R., Tung, Y-S., Wu, M.H., Zavalin, A., Wang, P.W., & Henderson, D.O. (2001). J. Phys.: Condens. Matter 13, 5535-5544.

Ueda, A., Wu, M.H., Aga, R., Meldrum, A., White, C.W., Collins, W.E., & Mu, R. (2007), Surface and Coating Technology 201, 85.

White, C.W.*et al.*(1989). Mat. Science Reports, 4, 43.

Weber, M.J., 1986, *Handbook of Laser Science and Technology*, CRC Press, ISBN: 0-8493-3507-8, Boca Raton, Florida (1986).42-8546.

Yager, T.A. & Kingery, W.D, (1981), Journals of Materials Science 16, 483; Yager, T.A. & Kingery, W.D. (1981). Journals of Materials Science 16, 489.

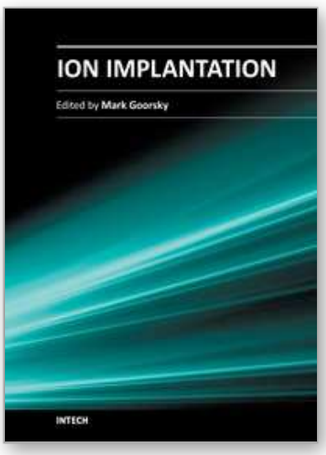

Ion Implantation

Edited by Prof. Mark Goorsky

ISBN 978-953-51-0634-0
Hard cover, 436 pages
Publisher InTech
Published online 30, May, 2012
Published in print edition May, 2012

Ion implantation presents a continuously evolving technology. While the benefits of ion implantation are well recognized for many commercial endeavors, there have been recent developments in this field. Improvements in equipment, understanding of beam-solid interactions, applications to new materials, improved characterization techniques, and more recent developments to use implantation for nanostructure formation point to new directions for ion implantation and are presented in this book.

InTech Europe
University Campus STeP Ri
Slavka Krautzeka 83/A
51000 Rijeka, Croatia
Phone: +385 (51) 770 447
Fax: +385 (51) 686 166
www.intechopen.com

InTech China
Unit 405, Office Block, Hotel Equatorial Shanghai
No.65, Yan An Road (West), Shanghai, 200040, China
中国上海市延安西路65号上海国际贵都大饭店办公楼405单元
Phone: +86-21-62489820
Fax: +86-21-62489821

IntechOpen